Chinese Journal of Aeronautics 24 (2011) 558-567

Contents lists available at ScienceDirect

Chinese Journal of Aeronautics

journal homepage: www.elsevier.com/locate/cja

# Modeling and Analysis of Helicopter Thermal and Infrared Radiation

PAN Chengxiong, ZHANG Jingzhou*, SHAN Yong

*College of Energy and Power Engineering, Nanjing University of Aeronautics and Astronautics, Nanjing 210016, China*

Received 21 September 2010; revised 19 November 2010; accepted 22 March 2011

**Abstract**

The temperature distributions on the helicopter airframe and in the exhaust plume are affected seriously by the engine exhaust system, rotor downwash and solar irradiance. To precisely simulate temperature distribution on the helicopter airframe and in the exhaust plume, the effects of rotor downwash and solar irradiance are considered in three-dimensional flow and heat transfer calculation under helicopter hovering. Based on the temperature distribution, a forward-backward ray tracing method is used to calculate the helicopter infrared (IR) radiation intensity. A numerical study is conducted on a fictitious helicopter model with an integrated exhaust system-tail airframe configuration, and the thermal and infrared radiation characteristics are analyzed.

*Keywords:* helicopter; infrared radiation; heat transfer; rotor downwash; solar radiation

## 1. Introduction

Infrared (IR) signature reduction is one of the most important elements that contribute in increasing the survivability of an aircraft, and hence reduces aircraft susceptibility to various forms of IR guided threats. There are two main infrared sources for a helicopter, one is the strong infrared emission in 3-5 μm wave band produced by exhaust nozzle and plume, the other is the helicopter skin contributing infrared emission in 8-14 μm wave band mainly. In order to reduce infrared signature and enhance survivability of helicopters, many means have been taken into consideration [1-7].

It is known that the temperature distributions on the fuselage skin and in the exhaust plume have a direct impact on IR signature of helicopters. Because the temperature distribution on fuselage skin is governed by heat transfer between skin and inner hot elements as well as skin and outer surrounding, there are many factors affecting the temperature distribution, such as the rotor downwash, heat radiation from engine casting, convective heat transfer between skin and cold air, solar irradiance on the skin, etc. On the other hand, the exhaust plume temperature distribution is seriously affected by the rotor downwash flow owing to the mixing action. In order to understand how downwash impacts plume temperature and ejecting capacity of helicopter exhaust systems, Zhang [4-5] and Huang [6-7], et al. conducted experimental investigations respectively. In these experiments, the downwash flow was simulated by a low-speed blower and downwash was evenly distributed. In the modeling of temperature distribution on helicopter skin, Zhang, et al. [8] carried out a study by setting some heat sources inside the helicopter body. These heat sources were assumed according to semi-experience, and solar irradiance was not taken into consideration.

In the present study, the effects of rotor downwash and solar irradiance are considered in flow and heat transfer calculation under helicopter hovering to precisely simulate temperature distributions on the helicopter skin and in exhaust plume. Based on the skin and plume temperature distributions, a forward-backward ray tracing method is used to calculate the infrared radiation intensity from the helicopter. A numerical

*Corresponding author. Tel.: +86-25-84895909.
*E-mail address:* zhangjz@nuaa.edu.cn
Foundation item: Funding of Jiangsu Innovation Program for Graduate Education (CXZZ11_0222)


doi: 10.1016/S1000-9361(11)60065-4

study is conducted for a fictitious helicopter model with an integrated exhaust system-tail airframe configuration. The thermal and infrared radiation characteristics on helicopter are analyzed.

## 2. Physical Model

The fictitious helicopter model is shown in Fig. 1. It is simply composed by six parts as head, pilot cabin, engine cabin, exhaust system, rotor plane and tail. The weight is supposed as 5 170 kg with 15 800 mm in length, 2 550 mm in width and 3 360 mm in height. The main rotor diameter is 13 800 mm, and the incidence angle of main rotor blade is fixed as 10° (that is the angle between blade chord line and wheel speed). The angle between the rotation axis and *y*-axis is 4°. The helicopter is powered by two turbo-shaft engines installed in both sides of helicopter airframe; each engine has an air mass flow of 2.5 kg/s and the exhaust gas temperature is 900 K. To make the engine exhaust nozzles (including lobed nozzles and mixing nozzles) invisible for infrared detector, hot exhaust nozzles are embedded inside exhaust system airframe of helicopter, as seen in Fig. 2. The exhaust gas is injected into mixing nozzle from lobed nozzle, then flows out from slot of mixing nozzle outlet near the side of exhaust system airframe. The flow section of mixing nozzle is transited from round to slot with 146 500 $mm^2$ inlet area and 229 000 $mm^2$ outlet area. The length-to-width ratio of outlet slot is 24. There is a pair of hatches on the top surface of exhaust system airframe to conduct the downwash flow into the exhaust system for cooling the exhaust nozzles and diluting hot exhaust plume. The exhaust system airframe wall is designed as both single and double layer. For the double-layer construction, the inner layer acts as a radiation emission shelter between the exhaust nozzles and outer layer of exhaust system airframe wall.

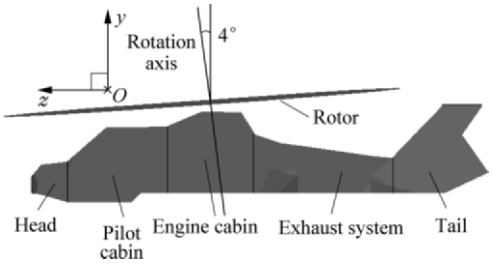


Fig. 1 Fictitious helicopter model viewed from *Oyz* plane.

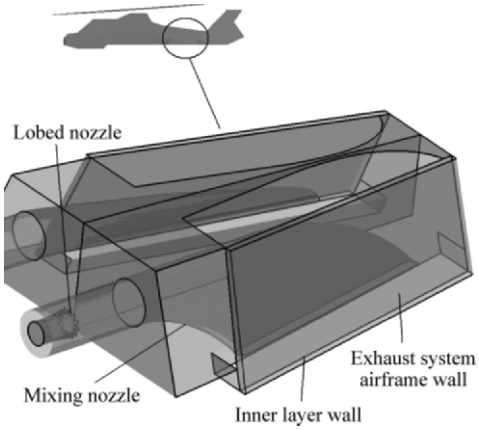


Fig. 2 Details of helicopter exhaust system.

## 3. Computation Method

The computation for helicopter thermal and infrared radiation includes two steps. Firstly, the flow and temperature fields are determined by the use of commercial computational fluid dynamics (CFD) software Fluent. Based on the skin and plume temperature distributions, a forward-backward ray tracing method is then used to calculate the infrared radiation intensity from the helicopter.

### *3.1. Flow and temperature fields*

#### 3.1.1. Governing equations

The flow and temperature fields of helicopter are very complicated. In the present study, the external flow around helicopter airframe originating from rotor downwash and internal flow inside exhaust nozzles originating from lobed nozzles are computed in a coupled mode to determine the temperature distributions on the helicopter skin and in exhaust plume. The governing equations include conservation of mass, momentum and energy equations, as well as species transport equation and radiative transfer equation. Those equations are listed as follows:

$$\nabla\cdot(\rho\boldsymbol{v})=0 \tag{1}$$

$$\rho(\boldsymbol{v}\cdot\nabla)\boldsymbol{v}=-\nabla p+\nabla\cdot\boldsymbol{\tau} \tag{2}$$

$$\nabla\cdot[\boldsymbol{v}(\rho E+p)]=\nabla\cdot[\lambda_{\text{eff}}\nabla T-\sum_j h_j\boldsymbol{J}_j] \tag{3}$$

$$\nabla\cdot(\rho\boldsymbol{v}Y_j)=-\nabla\cdot\boldsymbol{J}_j \tag{4}$$

$$\nabla\cdot[L(\boldsymbol{r},\boldsymbol{s})\boldsymbol{s}]+\alpha L(\boldsymbol{r},\boldsymbol{s})=\alpha\frac{\sigma T^4}{\pi} \tag{5}$$

where $\rho$ is density of gas, $\boldsymbol{v}$ velocity vector, $p$ static pressure, $\boldsymbol{\tau}$ stress tensor, $E$ total energy, $\lambda_{\text{eff}}$ effective conductivity ($\lambda_{\text{eff}}=\lambda+\lambda_t$, $\lambda$ is the thermal conductivity, and $\lambda_t$ the turbulent thermal conductivity), $T$ temperature; $h_j$ and $\boldsymbol{J}_j$ represent enthalpy and diffusion flux for species $j$ respectively; $Y_j$ is local mass fraction of species $j$, $L(\boldsymbol{r}, \boldsymbol{s})$ radiance, $\boldsymbol{r}$ position vector, $\boldsymbol{s}$ direction vector, $\alpha$ absorption coefficient, and $\sigma$ Stefan-Boltzmann constant.

To simulate the turbulence, eddy viscosity is determined according to the two equations SST $k$-$\omega$ turbulent model.

#### 3.1.2. Computational domain and boundaries

The computational domain is divided into two parts, the external flow around helicopter airframe originating from rotor plane and internal flow inside exhaust nozzles.

For the external flow, the helicopter is surrounded by a boundary more than 10 times of its rotor diameter and the pressure at that boundary is considered to be undisturbed atmosphere pressure approximately in the hovering state with a total pressure of 101 325 Pa and temperature of 283 K (see Fig. 3). The flow condition of rotor downwash is obtained from rotor downwash model (discussed in Section 3.2).

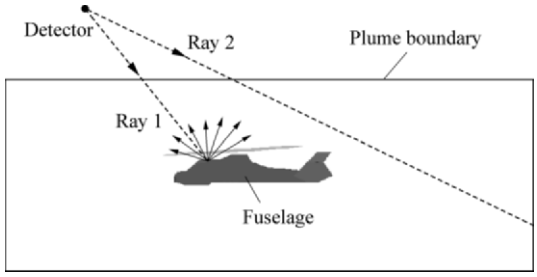


Fig. 3 Schematic of computation domain and detection.

For the internal flow inside exhaust nozzles originating from engine lobed nozzles, assuming the combustion in engine combustor is complete, so that the mass fraction of $N_2$, $CO_2$ and $H_2O$ in the exhaust gas could be obtained from kerosene reaction equation, they are 0.706, 0.209 and 0.085 respectively. The absorption coefficient of plume is 0.1 $m^{-1}$. At boundary surrounding the helicopter, the atmosphere is made of $N_2$ and $O_2$, and the mass fractions are 0.756 and 0.244 respectively.

Unstructured meshes to discretize the computational domain are adopted in the present research and about 5.5 million grids are used. The external flow and internal flow are computed in a coupled mode.

The walls of exhaust nozzles and helicopter airframe are set as fluid-solid coupling interfaces. The temperature on fluid-solid coupling interfaces is determined according to thermal equilibrium relationship. For examples, the heat transfer from exhaust plume to exhaust nozzle wall is balanced by radiative heat flux between exhaust nozzle wall and airframe inner wall. For the helicopter skin, the thermal equilibrium is associated with inner surface radiative heat flux, outer surface heat transfer to ambient, as well as solar irradiance obtained from solar irradiance model (discussed in Section 3.3).

### *3.2. Rotor downwash modeling*

As seen in Fig. 4, when the rotor blade rotates, the wheel speed of blade element is $\boldsymbol{u}=\boldsymbol{\omega r}$ (here $\boldsymbol{r}$ is the rotor radius and $\boldsymbol{\omega}$ is rotation speed). Here the angle $\phi$ between blade chord line and wheel speed is the incidence angle of rotor blade. Simultaneously the air is driven by the rotating blade to pass through the rotor plane with induced velocity $\boldsymbol{v}_i$. For a single blade element, the induced velocity is always perpendicular to the blade chord line. The wheel speed and induced speed compose the real velocity $\boldsymbol{w}$. And the angle between the blade chord line and real velocity direction is called the angle of attack $a$.

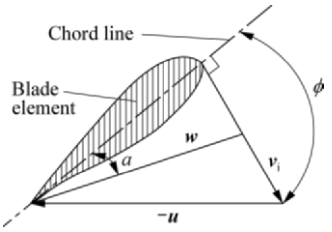


Fig. 4 Relationship between angles and velocities.

To provide a lift force to balance the helicopter's weight, rotor must pump the air against the direction of the lift. According to momentum theory [9] presumption that it is the momentum augmentation of the induced air that provides the lift force. Fig. 5 shows the air flowing through the rotation plane, where $V_0$ is the air flow velocity, $p'$ the static pressure in front of rotation plane, $\Delta p$ the total pressure augmentation through the rotation plane , and $a'$ and $b'$ represent model variables.

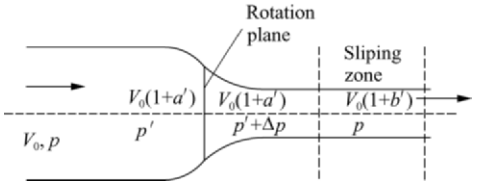


Fig. 5 Flow chart of air through rotation plane.

Supposing that the area of the rotation plane is $A$. The acting force on the air flow by the rotation plane is exactly the same as the lift force provided by the rotor in value but opposite in direction. It is equal to the momentum augmentation of air flow. The lift provided by this plane is [9]

$$F_t = G = A\Delta p = A\rho V_0^2 b'(1+a') \tag{6}$$

where $G$ represents the helicopter weight, $F_t$ the lift force.

For a helicopter in the hovering state, the lift force can be simplified as

$$F_t = G = 2\rho v_{i,\perp}^2 \pi R^2 \tag{7}$$

where $v_{i,\perp}$ is the magnitude of $\boldsymbol{v}_{i,\perp}$ which is the velocity component of $\boldsymbol{v}_i$ and perpendicular to the rotation plane, and $R$ the radius of the rotating blade.

Experimental measurement indicates that the magnitude of induced velocity $v_i$ is not simply linearly increased from 0 m/s at the centre of the rotation plane to $v_{i,max}$ at the edge [10-11]. Actually $v_{i,max}$ occurs at 80% of the blade radius, so that it is assumed that $v_i$ linearly increases from 0 m/s at the centre of the rotation plane to $v_{i,max}$ at 80% of the blade radius and then decreases linearly to 0 m/s to the edge. Thus the air mass flow through the rotation plane could be deduced:

$$\dot{m} = \int_0^{0.8R} 2\rho\pi \frac{v_{\mathrm{i,max},\perp}}{0.8R} r^2 \mathrm{d}r + \int_{0.8R}^{R} 2\rho\pi \frac{v_{\mathrm{i,max},\perp}}{0.2R}(R-r) r \mathrm{d}r \tag{8}$$

where $v_{\mathrm{i,max},\perp}$ is the vertical component magnitude of $\boldsymbol{v}_{\mathrm{i,max}}$.

Considering the relationships between angles and velocities in Fig. 4, there is the following expression:

$$v_{\mathrm{i},\perp} = v_{\mathrm{i}} \cos\phi \tag{9}$$

From Eqs. (7)-(9), the exact distribution and value of the induced velocity are determined if given the helicopter weight and rotor parameters. In this paper, the induced velocity distribution is used as velocity condition and is loaded into the commercial CFD solver through user-defined function to simulate the features of the downwash.

### 3.3. Solar irradiance modeling

Fig. 6 shows the schemematic of a solar beam raying on a wall surface. The horizontal plane is denoted by east (E), west (W), south (S) and north (N). A solar beam is vectored with altitude angle $\gamma$ and azimuth angle $\beta$, where $\gamma$ is the angle between beam ray and its projection on horizontal plane, and $\beta$ the angle between ray projection and south line.

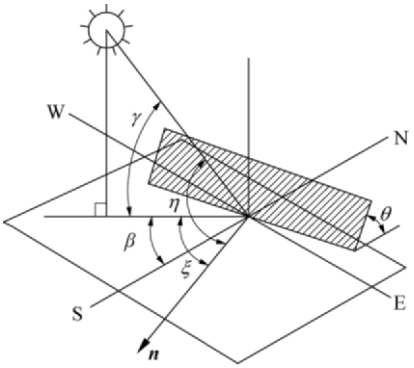


Fig. 6 Relationships between those angles.

For an arbitrary wall surface with inclination angle of $\theta$ to the horizontal plane, the normal line is denoted as $\boldsymbol{n}$. The angle between solar ray and $\boldsymbol{n}$ is called solar incidence angle $\eta$. Denoting the angle between solar ray projection and $\boldsymbol{n}$ as $\xi$, there is the following relationship.

$$\cos\eta = \cos\theta \sin\gamma + \sin\theta \cos\gamma \cos\xi \tag{10}$$

An isotropic sky solar irradiance model is adopted to predict the illumination energy source that results from solar irradiance [12-15]. The total solar irradiance $E_{\mathrm{T}\theta}$ on the wall surface includes three parts:

$$E_{\mathrm{T}\theta} = E_{\mathrm{D}\theta} + E_{\mathrm{d}\theta} + E_{\mathrm{R}\theta} \tag{11}$$

where $E_{\mathrm{D}\theta}$ is direct solar irradiance by solar rays, $E_{\mathrm{d}\theta}$ diffusive solar irradiance scattered by sky, $E_{\mathrm{R}\theta}$ reflective solar irradiance reflected from the ground [16].

$$E_{\mathrm{D}\theta} = E_0 P^M \cos\eta \tag{12}$$

$$E_{\mathrm{d}\theta} = \frac{1}{4} E_0 \frac{1-P^M}{1-1.4\ln P}(1+\cos\theta)\sin\gamma \tag{13}$$

$$E_{\mathrm{R}\theta} = \frac{1}{2} E_0 \rho_{\mathrm{g}} (1-\cos\theta)\left( P^M \sin\gamma + \frac{1}{2}\cdot\frac{1-P^M}{1-1.4\ln P}\sin\gamma \right) \tag{14}$$

where $E_0$ is solar constant, $P$ atmosphere transparency, $M$=1/sin $\gamma$, and $\rho_{\mathrm{g}}$ the reflectivity of the ground.

The helicopter skin is divided into many individual wall surfaces, by performing a face-to-face shelter analysis to determine the solar irradiance on all boundary faces. The heat flux from solar irradiance is then taken as a boundary heat source for the specific face to solve the temperature distribution on helicopter skin.

In this paper, the helicopter is assumed locating at north latitude 23° and east longitude 116°. The time is one noon of September under fair weather conditions. The direct solar irradiance is 1 250 W/m$^2$, and diffusive and reflective solar irradiance is totally 200 W/m$^2$ predicted by solar load calculator in Fluent software according to the location and weather conditions mentioned above.

### 3.4. Infrared signature

Because helicopter infrared radiation emits in the whole hemisphere, only a small part of it reaches detector at last. To enhance the calculation efficiency, a forward-backward ray tracing method is adopt to calculate the infrared intensity from the helicopter in 3-5 μm and 8-14 μm bands [17-18].

In the forward ray tracing process, each ray originating from detector interacts with exhaust plume or helicopter skin (such as Ray 1 and Ray 2 in Fig. 3) or departs the computational domain. If the ray reaches plume boundary, the tracing process is over. If the ray reaches wall element $i$, then this ray will be divided into reflective rays evenly deployed in the whole hemisphere dimension as displayed in Fig. 3 and continuous tracing will be done to find if those reflective rays re-intersect with other wall elements. If its reflex have $m$ intersections with other wall elements, then the irradiance from those walls on wall $i$ is

$$H_{\sigma,i} = \sum_{j=1}^{m} \int_{\Omega_j} L_{\sigma,j} \cos\vartheta_j \mathrm{d}\Omega \tag{15}$$

where $L_{\sigma j}$ is radiance of wall element $j$, $\vartheta_j$ the angle between the line connecting element $j$ and element $i$ and the normal line of element $i$, and $\Omega$ the solid angle from element $j$ to element $i$. Thus radiance of wall element $i$ is

$$L_{\sigma,i} = \varepsilon_i L_{\mathrm{b},\sigma}(T_i) + \frac{1-\varepsilon_i}{\pi} H_{\sigma,i} \tag{16}$$

where the first term on the right side is the radiance of wall element $i$ by itself, the second term the reflection of radiance from other wall elements to wall element $i$, and $\varepsilon_i$ the emissivity of wall element $i$, $L_{\mathrm{b},\sigma}(T_i)$ the ra-

diance of black body at the temperature of wall element *i*.

The backward process begins at the last intersection point that ray arrives. In the calculation of energy transmitting process of the backward ray in a given direction *l*, the following radiation transfer equation is used for absorbing-emitting medium:

$$\frac{\mathrm{d}L_\sigma}{\mathrm{d}l} = -k_{\alpha\sigma}(L_\sigma - L_{\mathrm{b},\sigma}) \tag{17}$$

where $k_{\alpha\sigma}$ is spectrum absorption coefficient, and $L_\sigma$ spectrum radiance in direction *l*.

After backward tracing has been done along all recorded rays, the heat flux of irradiance received by detector can be expressed by

$$H = \sum_{j=1}^{N_\mathrm{B}} \sum_{i=1}^{N} L^n_{\sigma,(i,j)} \cos\vartheta_i \, \Delta\Omega_i \, \Delta\delta_j \tag{18}$$

where $N_\mathrm{B}$ is the total band number, $N$ the number of recorded rays, $L^n_{\sigma,(i,j)}$ spectrum radiance at the *j*th band number and the *i*th ray, $\vartheta_i$ the angle between ray and the normal of wall *i*, $\Delta\Omega_i$ the solid angle of *i*th ray, and $\Delta\delta_j$ the spectrum interval. Because the helicopter is regarded as a point target for the detector, the radiation intensity of the target can be expressed as

$$I = HZ^2 \tag{19}$$

where *Z* is the distance between detector and helicopter.

## 4. Results and Discussion

### *4.1. Flow field and temperature distribution*

Fig. 7 shows the comparison of flow temperature distributions at the exit of exhaust nozzles between experimental data [19] and simulation (here *X* represents the distance along exit length direction and *D* the inlet diameter of the mixing nozzle). From Fig. 7 it is quite clear that present computational method fits well with experimental result. The temperature is relatively lower at the front of exhaust exit while higher at the far end. The reason is probably that the internal flow affected by centrifugal force insides curved exhaust nozzles (as seen in Fig. 8 obtained by computation). The plume temperature is not distributed evenly at the exit.

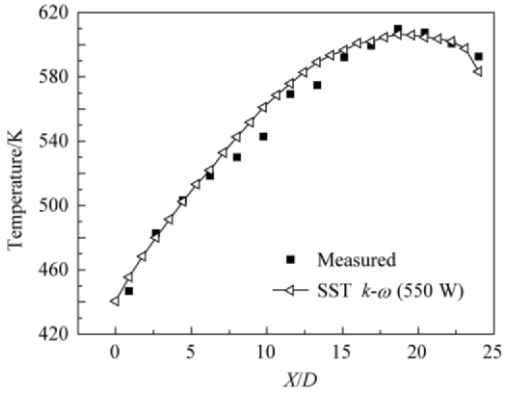


Fig. 7 Flow temperature distributions at exhaust nozzles exit.

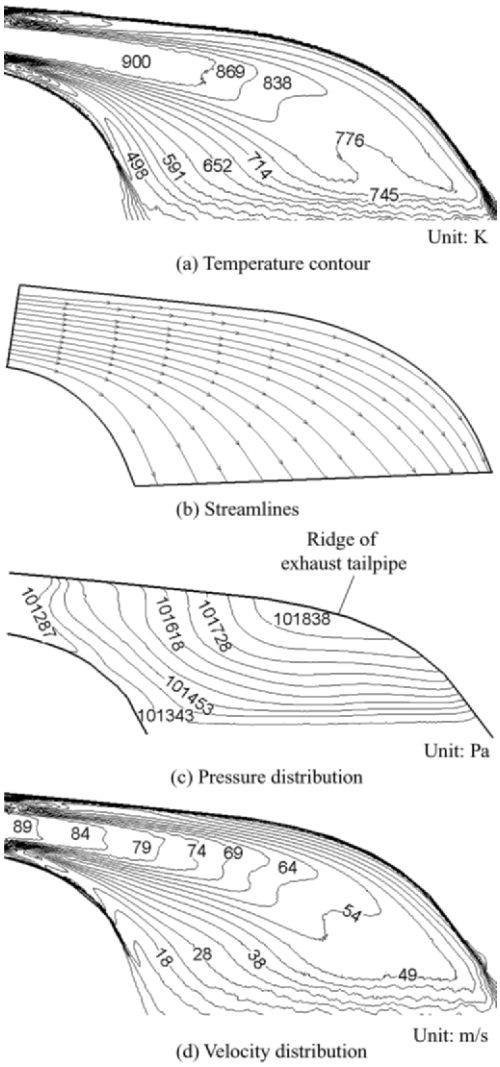


Fig. 8 Flow fields inside exhaust nozzles.

Fig. 9 shows the temperature distributions at the ridge of exhaust nozzles (here $X'$ represents distance away from the inlet of exhaust nozzles). It should be noted that the downwash is simulated by a fan in experiment. As the downwash velocity varies from 0 m/s to 20 m/s, the wall temperature of the exhaust nozzles decreases. According to the rotor downwash modeling presented in Section 3.2, the downwash average velo-

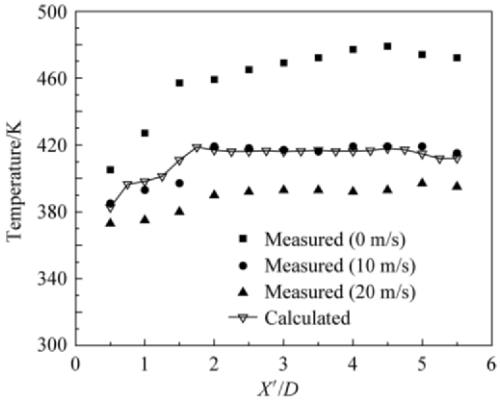


Fig. 9 Temperature distributions at ridge of exhaust nozzles.

city is about 12 m/s, which resembles the evenly 10 m/s downwash in the experiment.

Fig. 10 shows temperature contour and streamline in a section plane of exhaust system. The plume temperature contours and streamlines are not symmetrical because tangent component of downwash velocity has a deflection effect on them. With the slot outlet structure of mixing nozzle, hot exhaust plume dissipates quite fast into atmosphere, as can be noticed from Fig. 10(b).

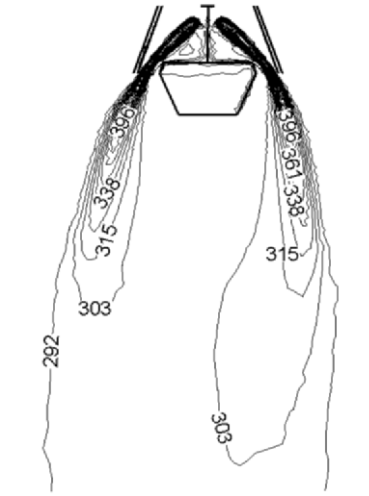


(a) Temperature contour of exhaust system

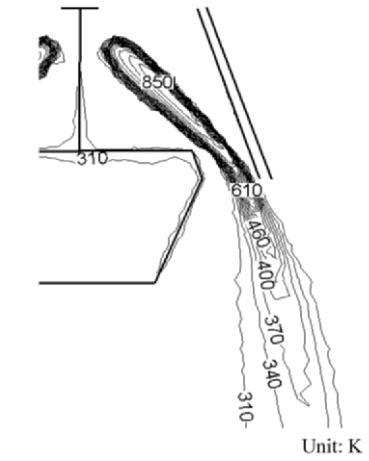


(b) Temperature contour of exhaust system with a closer look

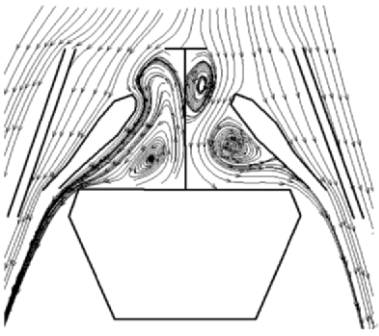

(c) Streamlines of exhaust system

Fig. 10 Flow fields in a section plane of exhaust system airframe.

Figs. 11-13 display temperature contour on exhaust system without the impact of direct solar irradiance (on shadow side). Although the inner layer and airframe wall have no direct contact with the hot nozzles or plume, they are still several degrees higher than the surrounding temperature due to radiative heat transfer between airframe wall and exhaust nozzles embedded inside exhaust system. It is quite clear that with inner layer wall as a radiation emission shelter, airframe wall is mildly heated by hot nozzles embedded inside exhaust system. Even with airframe emissivity $\varepsilon = 0.8$, the fuselage is only 4 K hotter than surrounding temperature when inner layer wall exists. When there is no inner layer to shelter hot parts inside exhaust system, airframe wall is more than 10 K higher even with $\varepsilon = 0.2$. As the emissivity gets higher, for airframe without inner layer, fuselage temperature rises distinctively.


(a) Without innner layer


(b) With innner layer

| Number | Temperature/K |
|---|---|
| 12 | 322 |
| 11 | 318 |
| 10 | 315 |
| 9 | 311 |
| 8 | 308 |
| 7 | 304 |
| 6 | 301 |
| 5 | 297 |
| 4 | 294 |
| 3 | 290 |
| 2 | 287 |
| 1 | 283 |

Fig. 11 Temperature contour on exhaust system with $\varepsilon = 0.2$.

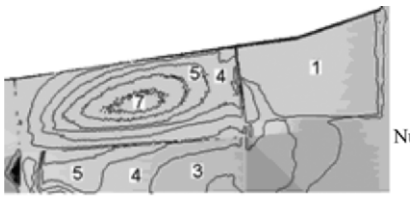


(a) Without innner layer


(b) With innner layer

| Number | Temperature/K |
|---|---|
| 12 | 322 |
| 11 | 318 |
| 10 | 315 |
| 9 | 311 |
| 8 | 308 |
| 7 | 304 |
| 6 | 301 |
| 5 | 297 |
| 4 | 294 |
| 3 | 290 |
| 2 | 287 |
| 1 | 283 |

Fig. 12 Temperature contour on exhaust system with $\varepsilon = 0.5$.

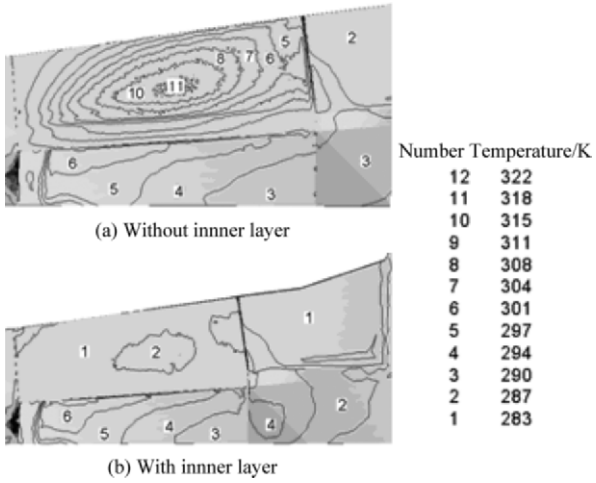


Fig. 13 Temperature contour on exhaust system with $\varepsilon = 0.8$.

Fig. 14 displays temperature contour on a helicopter fuselage under solar irradiance from left with inner layer wall. Because the temperature labels are exactly the same as those in Figs. 11-13, they are omitted here to spare some room for a clearer display of temperature distribution on airframe. It can be noticed that the temperature on the direct solar irradiance side is obviously much higher than the shadow side. As the emissivity rises, the solar irradiance heating effect becomes quite obvious. The temperature difference at some parts of fuselage is about 11, 25, 35 K respectively as airframe emissivity rises from 0.2 to 0.8, which is quite enough to make a difference in infrared radiation intensity.

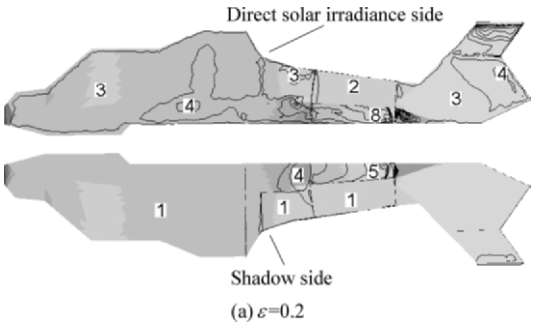


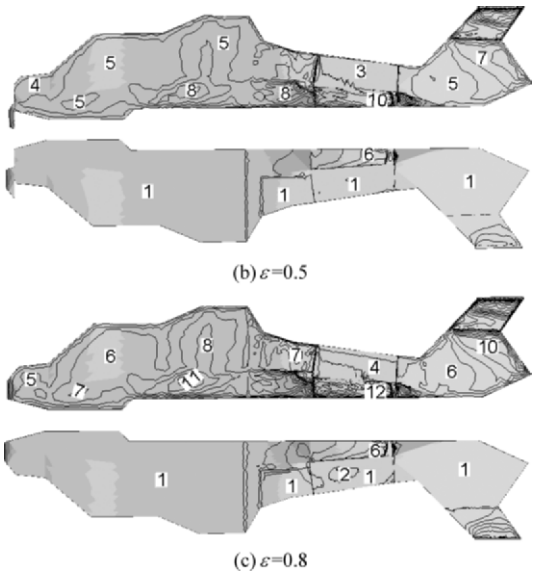


Fig. 14 Temperature contour on helicopter skin.

Table 1 shows the averaged temperature on head, pilot cabin, engine cabin and tail with inner layer at three kinds of emissivity respectively. The maximum difference is about 6, 15, 20 K respectively on helicopter skins with $\varepsilon = 0.2$, 0.5, 0.8 because lower emissivity means less solar irradiance energy would be absorbed.

**Table 1 Averaged temperature on certain parts**

| Condition | | Average temperaure/K | | | |
|---|---|---|---|---|---|
| | | Head | Pilot cabin | Engine cabin | Tail |
| $\varepsilon = 0.2$ | Direct solar irradiance side | 286.9 | 288.1 | 289.7 | 289.8 |
| | Shadow side | 283.4 | 283.2 | 283.3 | 283.5 |
| $\varepsilon = 0.5$ | Direct solar irradiance side | 292.2 | 294.9 | 298.2 | 297.4 |
| | Shadow side | 283.8 | 283.6 | 283.8 | 284.1 |
| $\varepsilon = 0.8$ | Direct solar irradiance side | 296.8 | 300.7 | 305.1 | 304.2 |
| | Shadow side | 284.5 | 284.2 | 284.6 | 284.7 |

### *4.2. Infrared radiation intensity distribution*

In the following part, the infrared radiation intensity characteristics in 3-5 μm band and 8-14 μm band of the helicopter will be discussed in *Oxz* plane. A forward-backward ray tracing method is adopted as discussed in Section 3.3. A thorough comparison between predicted data with this method and experimental results can be found in Ref. [18]. In that plane 36 infrared radiation intensity detectors are uniformly deployed on a circle which is 100 m away in radius from the helicopter. In order to preserve the original characteristics of the helicopter infrared radiation intensity, the affects of atmosphere attenuation are ignored.

Figs. 15-16 show 3-5 μm and 8-14 μm bands infrared radiation intensity characteristics of the helicopter airframe with $\varepsilon$=0.8. It can be seen that airframe radiation intensity is not apparently impacted with or without inner layer of exhaust system wall. The most difference is within 5% in 3-5 μm band while in 8-14 μm

band the difference is even less. The same is true with cases of airframe with $\varepsilon = 0.2$, 0.5, which explains why their results are omitted here. It is probably because the projected area of the exhaust system airframe only takes about 30% in the total helicopter fuselage so that the temperature difference on it does not impact full airframe infrared intensity severely. Another interesting phenomenon worth mentioning is that infrared radiation intensity distribution of the helicopter is not symmetrical due to solar irradiance. The infrared radiation intensity on the side facing direct solar incidence is bigger than the shadow side for helicopter airframe with $\varepsilon$=0.8 by 100% and 33% in 3-5 μm and 8-14 μm bands respectively. It is quite clear that solar irradiance rather than inner layer wall has a dominant impact on the airframe infrared radiation intensity distribution because solar irradiance will raise the whole fuselage temperature while inner layer wall can just impact exhaust system.

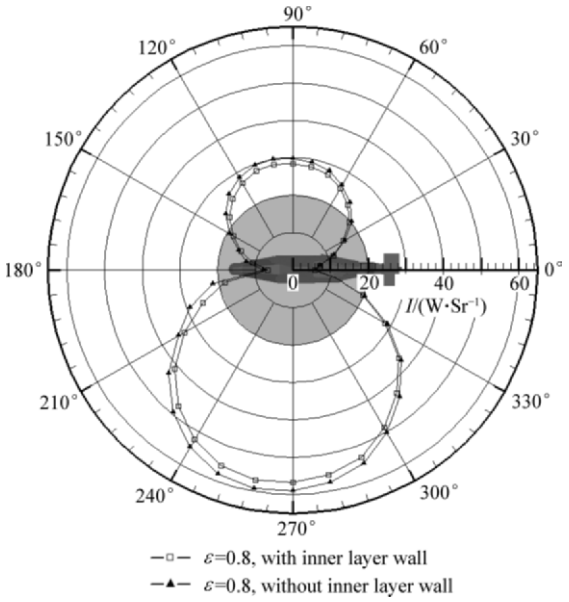


Fig. 15 3-5 μm band infrared radiation intensity characteristics of helicopter airframe with $\varepsilon = 0.8$.

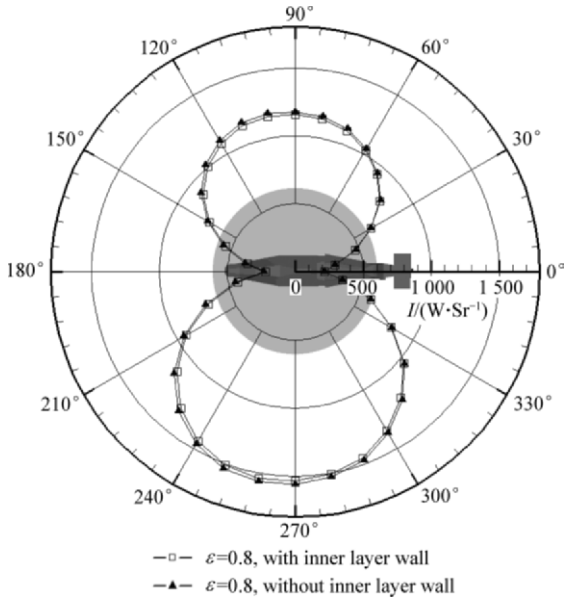


Fig. 16 8-14 μm band infrared radiation intensity characteristics of the helicopter airframe with $\varepsilon = 0.8$.

To let readers have a more clear understanding on those differences, the airframe infrared radiation intensity on 90° azimuth angle (represents shadow side) and 270° azimuth angle (represents direct solar irradiance side) are listed in Table 2.

**Table 2 Infrared radiation intensity of helicopter airframe with or without inner layer wall**

| Condition | | $I$/(W·Sr$^{-1}$) | | | |
|---|---|---|---|---|---|
| | | With inner layer wall | | Without inner layer wall | |
| | | 90° azimuth angle | 270° azimuth angle | 90° azimuth angle | 270° azimuth angle |
| $\varepsilon = 0.2$ | 3-5 μm | 6.630 68 | 8.301 9 | 6.681 79 | 8.374 73 |
| | 8-14 μm | 281.081 | 308.091 | 282.077 | 309.503 |
| $\varepsilon = 0.5$ | 3-5 μm | 16.989 9 | 27.935 9 | 17.618 6 | 28.823 2 |
| | 8-14 μm | 709.812 | 869.199 | 719.189 | 880.895 |
| $\varepsilon = 0.8$ | 3-5 μm | 28.335 | 56.810 6 | 29.770 7 | 58.993 2 |
| | 8-14 μm | 1 154.32 | 1 533.11 | 1 174.05 | 1 558.93 |

Fig. 17 shows infrared spectral radiation intensity characteristics of the helicopter airframe with $\varepsilon = 0.8$ at azimuth angles of 90° and 270°. At 270° azimuth angle, the maximum spectral radiation intensity happens at wavelength 9.524 μm which means the effective radiative temperature of fuselage with direct solar irradiance is about 304 K according to Wien Displacement Law. While at 90° azimuth angle the effective radiative temperature of fuselage is about 286 K. This agrees very well with the data shown in Table 1 which means results predicted by the forward-backward ray tracing method are quite valid.

Figs. 18-19 shows 3-5 μm and 8-14 μm bands infrared radiation intensity characteristics of the helicopter airframe with $\varepsilon = 0.2$, 0.5, 0.8 respectively. All of them are structures with inner layer wall. As fuselage emissivity rises, infrared radiation intensity becomes higher in both 3-5 μm and 8-14 μm bands. In 3-5 μm band when fuselage emissivity rises from 0.2 to 0.8, infrared radiation intensity is 4.3 times on direct solar irradiance side and 6.8 times on shadow side respectively. In 8-14 μm band, it is 4.1 and 4.9 times respectively.

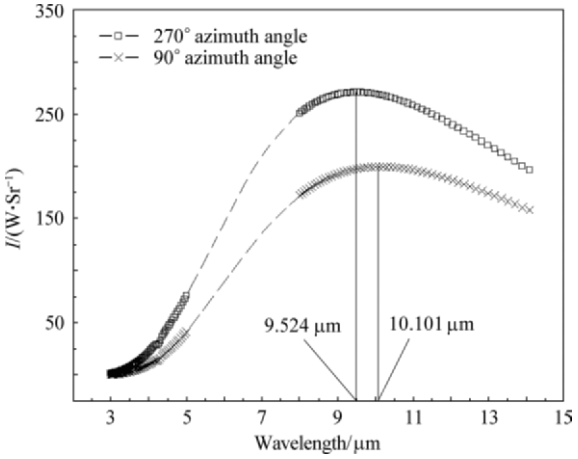


Fig. 17 Infrared spectral radiation intensity of helicopter airframe with $\varepsilon = 0.8$ at two special azimuth angles.

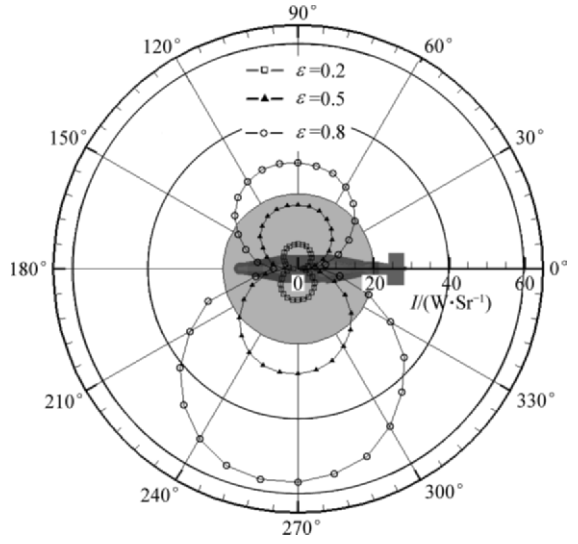


Fig. 18 3-5 μm band infrared radiation intensity characteristics with inner layer wall.

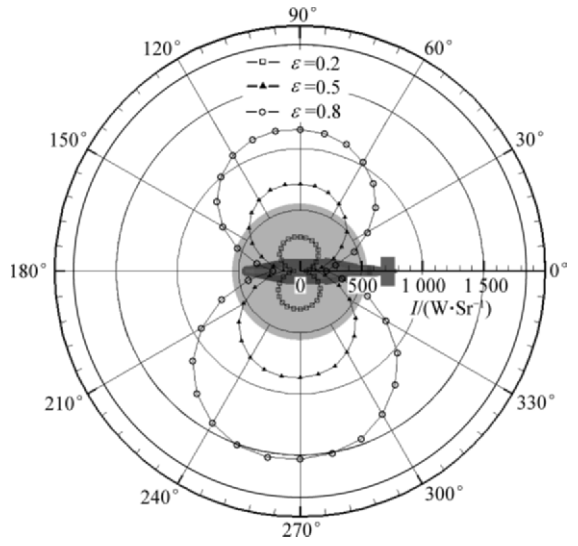


Fig. 19 8-14 μm band infrared radiation intensity characteristics with inner layer wall.

To check airframe infrared radiation intensity data with three kinds of emissivity closely, readers can resort to the first two lines in Table 2.

## 5. Conclusions

(1) Tangent component of downwash velocity has a deflection effect on temperature contour of exhaust plume and vortexes inside exhaust system airframe.

(2) With inner layer wall as a radiation emission shelter, airframe wall is mildly impacted by hot nozzles embedded inside exhaust system while heating effect is more obvious when there is no inner layer.

(3) The temperature on the direct solar irradiance side is obviously much higher than the other side. The maximum and averaged temperature differences at some parts is about 35 K and 20 K respectively.

(4) Infrared radiation intensity distribution of the helicopter is not symmetrical due to solar irradiance while is not apparently impacted with or without inner layer of exhaust system wall. The infrared radiation intensity on the side facing direct solar incidence is bigger than the shadow side for helicopter airframe with $\varepsilon = 0.8$ by 100% and 33% in 3-5 μm and 8-14 μm bands respectively.

(5) Once the fuselage emissivity is reduced from 0.8 to 0.2, the maximum infrared radiation intensity could be suppressed by about 75%.

## References

**[1]** Power G D, McClure M D, Vinh D. Advanced IR suppressor design using a combined CFD/test approach. AIAA-1994-3215, 1994.

[2] Rao G A, Mahulikar S P. Integrated review of stealth technology and its role in airpower. The Aeronautical Journal 2002; 106(1066): 629-641.

[3] Mahulikar S P, Sonawane H R, Rao G A. Infrared signature studies of aerospace vehicles. Progress in Aerospace Sciences 2007; 43(7-8): 218-245.

[4] Shan Y, Zhang J Z, Li L G. Numerical calculation and experimental verification for the infrared radiation characteristics of helicopter infrared radiation suppressor. Journal of Infrared and Millimeter Waves 2006; 25(2): 96-100. [in Chinese]

[5] Zhang J Z, Shan Y, Li L G. Investigation on lobed nozzle mixer-ejector infrared suppressor for helicopter exhaust system. Acta Aeronautica et Astronautica 2007; 28(1): 32-36. [in Chinese]

[6] Zhu Y, Huang Y. Experimental investigation of exit temperatures of an infrared suppressor model. Journal of Aerospace Power 2007; 22(7): 1142-1147. [in Chinese]

[7] Wang X W, Huang Y, Lu Y X. Influences of the downwash flow from a helicopter rotor on the performances of an infrared suppressor. Journal of Aerospace Power 2003; 18(6): 772-776. [in Chinese]

[8] Zhang Q, Cao Y H. An engineering method to calculate temperature field of helicopter. Aeronautical Computer Technique 2005; 35(2): 36-38. [in Chinese]

[9] Liu P Q. Aero-propeller theory and applications. Beijing: Beihang University Press, 2006. [in Chinese]

[10] Kang N, Sun M. Navier-Stokes calculations of induced velocity of a rotor in forward flight with ground effects. Acta Aerodynamica Sinica 1998; 16(2): 221-225. [in Chinese]
[11] Wang B. Numerical simulation and analysis of helicopter rotor/fuselage flow field based on CFD method. MS thesis, Nanjing University of Aeronautics and Astronautics, 2007. [in Chinese]
[12] Gueymard C A. Direct and indirect uncertainties in the prediction of tilted irradiance for solar engineering applications. Solar Energy 2009; 83(3): 432-444.
[13] Loutzenhiser P G, Manz H, Felsmann C, et al. Empirical validation of models to compute solar irradiance on inclined surfaces for building energy simulation. Solar Energy 2007; 81(2): 254-267.
[14] Wang Z Y, Lu Y Q, Peng Q S, et al. An infrared image synthesis model of city building based on meteorology and heat transfer. Acta Simulata Systematica Sinica, 2000; 12(5): 517-523. [in Chinese]
[15] Huang X H, Bi X P. Calculation and analysis of infrared radiation temperature for the tank power compartment armored plate. Opto-Electronic Engineering 2009; 36(7): 89-93. [in Chinese]
[16] Yunnan College of Forestry. Meteorology. Beijing: Agriculture Press, 1979. [in Chinese]
[17] Johansson M, Dalenbring M. SIGGE, a prediction tool for aeronautical IR signatures, and its applications. AIAA-2006-3276, 2006.
[18] Shan Y, Zhang J Z. Numerical investigation of flow mixture enhancement and infrared radiation shield by lobed forced mixer. Applied Thermal Engineering 2009; 29(17-18): 3687-3695.
[19] Pan C X, Zhang J Z, Shan Y. Modeling and analysis of helicopter skin temperature distributions. Acta Aeronautica et Astronautica Sinica 2011; 32(2): 249-256. [in Chinese]

## Biographies:

**PAN Chengxiong** Born in 1985, he received B.S. degree from Nanjing University of Aeronautics and Astronautics in 2008 and then became a Ph.D. candidate there. His main research interests are infrared stealth and heat transfer.
E-mail: chengxiong_pan@yahoo.com.cn

**ZHANG Jingzhou** Born in 1964, He is the professor and supervisor of Ph.D. candidates. His main research interests are heat transfer, combustion and infrared stealth technology.
E-mail: zhangjz@nuaa.edu.cn